JGR Space Physics

RESEARCH ARTICLE
10.1029/2020JA027843

Improved Analysis of STEVE Photographs

Charles L. Bennett[1] and **Notanee Bourassa**[2]

[1]Retired From Lawrence Livermore National Laboratory, Livermore, CA, USA, [2]Saskatchewan Aurora Hunters, Saskatchewan, Canada

Key Points:

- A method for accurate registration and synchronization of digital photographs of strong thermal emission velocity enhancement (STEVE) is presented
- The nature of the flux producing STEVE emissions can be quantified from such photographs using a model for auroral precipitation
- It is found that the STEVE green picket fence and purple bands share magnetic field lines

Supporting Information:

Supporting Information may be found in the online version of this article.

Correspondence to:

C. L. Bennett,
Charlie_Bennett@comcast.net

Citation:

Bennett, C. L., & Bourassa, N. (2021). Improved analysis of STEVE photographs. *Journal of Geophysical Research: Space Physics*, *126*, e2020JA027843. https://doi.org/10.1029/2020JA027843

Received 23 JAN 2020
Accepted 25 NOV 2020

Abstract We present a new approach for the analysis of high-resolution digital camera photographs taken by photographers who have fortuitous been able to capture rare events, such as the glowing sky phenomenon known as strong thermal emission velocity enhancement (STEVE). This method is especially effective with a time lapse series of images of the night sky taken under constant camera settings with a steady pointing. Stars, planets, and satellites seen in such images can be used to determine the precise and accurate registration of camera pixels to coordinates of angular altitude and azimuth. The location of satellites in the image enables precise and accurate synchronization of the images. We apply these techniques to the series of photographs of STEVE taken on July 25, 2016. We confirm the altitude structure previously found for STEVE. We find it most likely that the green picket fence features often seen during STEVE events are produced by auroral electron precipitation. With the precipitation assumption, we are able to extract novel information about the energy spectrum of the particles responsible for the production of STEVE luminosity in this particular event. Similarly, analyses of archived digital photographs may constitute a treasure trove of important data for improved understanding of rare and transient events, such as STEVE.

Plain Language Summary Extremely rare events are sometimes captured in photographs by people who just happen to be in the right place and at the right time to notice something unusual happening in the night sky. Modern digital cameras can have such high pixel counts and sensitivity that such photographs can contain unique and valuable information. The location of stars, planets, and even occasional satellites in these images can be used to precisely interpret the timing and location of the events captured in the pictures. The methods described and computer software included in this paper can be used to make such analysis easier. The mysterious phenomenon known as strong thermal emission velocity enhancement (STEVE) is one example of such a rare event that appears as a long and narrow streak of purple light, sometimes extending from horizon to horizon, just to the south of the Northern lights. Since STEVE was first discovered, it has been unclear what the connection is between STEVE and the Northern lights. Using the methods described here, we find strong evidence that the mechanisms producing the Northern Lights and STEVE are very closely related.

1. Introduction

The nighttime optical phenomenon STEVE was originally noticed and named by a network of enthusiastic auroral photographers. The initial publication in the scientific literature discussing this phenomenon by MacDonald et al. (2018), observed the correlation between Steve and subauroral ion drift (SAID) and created the backronym "strong thermal emission velocity enhancement" (STEVE). A typical STEVE event appears as a narrow purple band of predominantly east-west oriented light, located equatorward of concurrent auroral activity and may extend from horizon to horizon. Sometimes, in addition to the purple band, intermittent green streaks, known as the "picket fence" are also seen. The question as to whether STEVE is produced by particle precipitation or ionospheric skyglow was raised very early by Gallardo-Lacourt et al. (2018), and still remains a topic of debate.

In Archer et al. (2019) and Chu et al. (2019), the vertical distribution of the optical emissions from a STEVE event on September 16, 2016 was determined. In this event, the green picket fence structures were aligned with the geomagnetic field and extended from 95 to 150 km. The purple band of STEVE extended between 130 and 270 km and was found to extend vertically along similar magnetic field lines to the picket fence features.

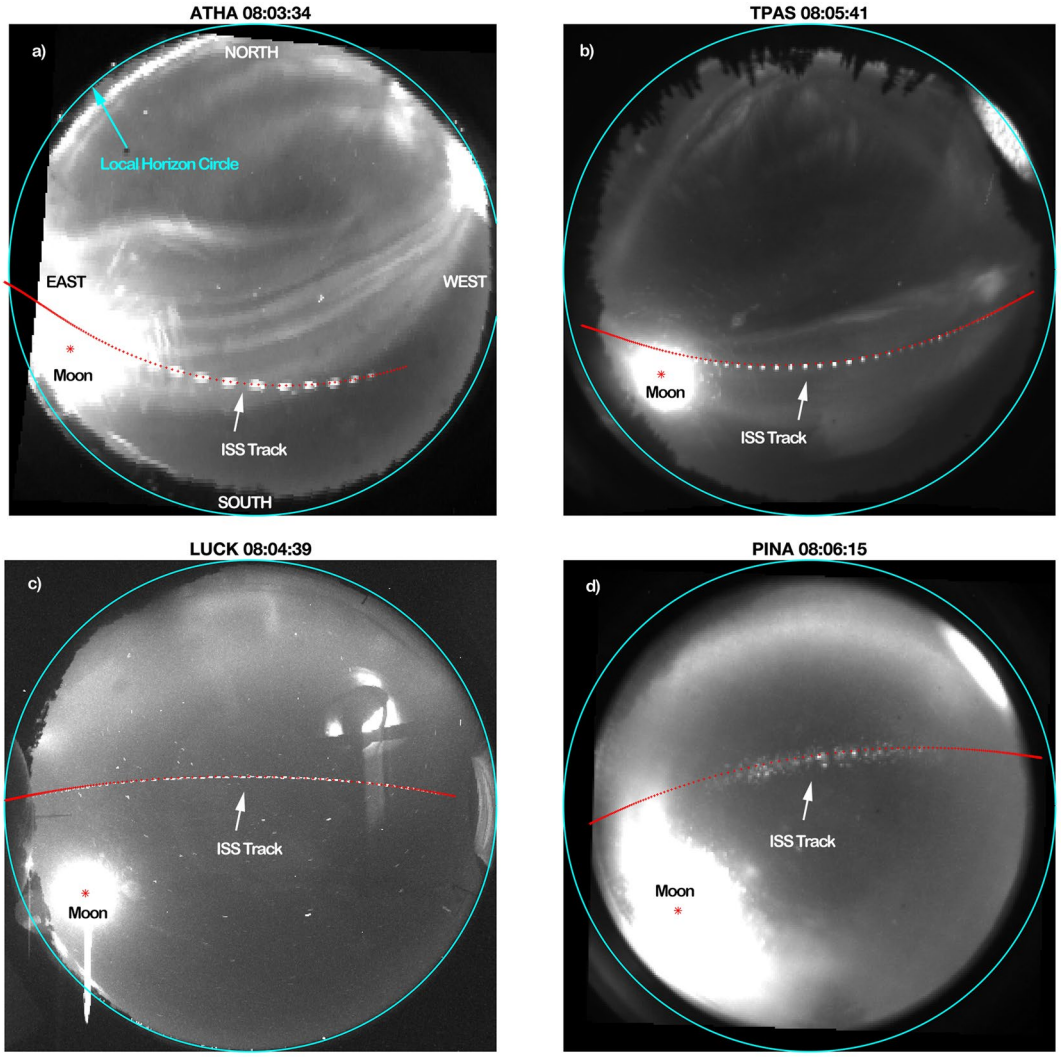

Figure 1. For the ATHA, TPAS, LUCK, and PINA ASI imagers, a Maxima Merged "MM" composite image (described further in the text) from a number of camera frames nearest the local meridian crossing time of the ISS is shown. The ISS location in the ASI imagers computed from its orbital elements is indicated by a series of red dots corresponding to the ISS location at three second intervals. The three s interval chosen represents the cadence of the LUCK and TPAS cameras. Each image's title time is chosen to be the frame time closest to the meridian crossing of the ISS over the respective ground station. The frame time for each ASI corresponds to the time at the end of each camera's exposure. In these MM composite images, the ISS shows up as a bright "dashed line" in each image, with the dash length proportional to the exposure time for each ASI frame (five s for ATHA, two s for LUCK, and one s for both TPAS & PINA). With perfect synchronization, the leading end of each "dash" should line up with a red dot.

Spectroscopic observations by Gillies et al. (2019) of a April 10, 2018 STEVE event found the green picket fence structure to be associated with strong OI (557.7 nm) emission. In contrast, the purple band was found to have a spectrum very similar to the ambient airglow, and approximately equal in intensity, thus locally doubling the airglow along the brightest portions of the purple band. This is most clearly seen in their Figure 1 by a comparison of the spectrum of STEVE with neighboring background pixels slightly poleward and equatorward. In Nishimura et al. (2019), it is suggested that electron precipitation could be a possible driver of the green picket fence features, if not the purple band structures. On the other hand, based on the presence of 5577 Å OI emission and near absence of N_2^+ first negative emission in one particular STEVE event (Mende, 2019) claim that this constitutes strong evidence against the hypothesis of precipitation.

Many of the scientific studies of Steve have exploited photographs taken by auroral photographers in conjunction with the more accurately calibrated network of All-Sky-Imager (ASI) photographs and satellite

observations. Although, these auroral photographers may sometimes be scientific professionals, quite often they are amateur photographers or auroral enthusiasts that happen to be in the right place at the right time. By virtue of the fortuitous proximity of the these photographers to the STEVE events they photographed, these photographs have extraordinarily high spatial resolution and sensitivity compared to the better calibrated ASI and space-based images, and we believe that they represent a significant reservoir of highly detailed data that could be very helpful to improve our understanding of STEVE. The network of "citizen scientists" organized by MacDonald et al. (2015) is particularly effective in this regard.

Here, we describe an improved method for the determination of the 3-d spatial structure of STEVE and more accurate temporal synchronization of such photographs for use in conjunction with ASI images and/or space-based data. We then apply this method to the July 25, 2016 event originally published by MacDonald et al. (2018). Finally, we demonstrate how the energy distribution and temporal behavior of the particles producing STEVE emissions may be extracted from such photographs. From the quality of the fits of observed green light emission to models, we believe this analysis bolsters the case that the green picket fence features of STEVE are produced by auroral electron precipitation.

2. Methodology

The July 25, 2016 STEVE event was photographed by N. Bourassa from a site near Regina Saskatchewan (REGI) with a Nikon D810 digital camera. Most of these images were taken with a sensitivity set to ISO 4000. The REGI RAW camera data was converted to 16-bit digital numbers using Nikon's Capture NX-D version 1.5.3 software (Nikon, 2019) with no adjustment applied to the colors. The readout noise of the D810 is approximately 3.8 electrons, with a dark current of 0.25 e/pixel/s at 30 °C according to (Lodriguss, 2020). As the Bourassa photographs were taken with the camera exposed to the cool evening air, although the temperature was not recorded, it was undoubtedly at a lower temperature than 30 °C, and thus the dark current is less than 1 e/pixel for the 4 s exposures discussed in this article. These readout noise and dark current levels are relatively insignificant compared to the "clutter" noise of intensity fluctuations due to faint stars, galaxies, and other celestial objects that are present in the Bourassa photographs.

Concurrent with these photographs published in MacDonald et al. (2018), although data was stored from 10 distinct ASI sites, relatively clear sky conditions were only available from the four Canadian sites at Lucky Lake (LUCK) in Saskatchewan, Athabasca (ATHA) in Alberta, Pinawa (PINA), and The Pas (TPAS) in Manitoba. The complete sequence of images from the ASI cameras are available for download from University of Calgary (2018). The details on the spatial resolution, spectral coverage and site location for these various cameras are tabulated in Table 1. The ASI data can be converted to absolute units of radiant intensity using a combination of a dark flat field and the sensitivity Rayleigh per Digital Number (R per DN) values.

2.1. Synchronization Using Bright Satellite Transits

In order to accurately triangulate the location of objects seen concurrently from multiple cameras, it is important to know both the location of each camera, and the time of each image. In the case of the ASI cameras, the geodetic coordinates are included in the meta-data associated with each image as well as a time stamp. On the other hand, the high-resolution images of STEVE sometimes available from fortuitous observations by auroral photographers do not always have such high accuracy location or time stamps. In the July 25, 2016 STEVE event examined here, the REGI site location is well remembered by N. Bourassa, and is clearly identifiable in some of the photographs, but we have found that the time stamp was off by 165 s. Although this error may be insignificant for the analysis of relatively slowly changing structures, the green picket fence features seen in STEVE are especially dynamic, and accurate time synchronization is important. For example, in the later REGI images taken at a 2 s cadence with 1 s exposure, there are significant motions and changes observable in the green picket fence "posts" from frame to frame. The first step in our method for accurate triangulation of structures between various sets of images is accurate correction of the time stamps associated with each image.

The orbits of bright low-earth orbit (LEO) satellites can be calculated with great accuracy (Aida, 2013) using twoline elements (TLEs) that are publicly available from Kelso (2019). As an example, the absolute location of the International Space Station (ISS) can be determined to within a few kilometers at any given time. As

Table 1
Image Registration Parameters

Site designator:	REGI	LUCK	ATHA	TPAS	PINA
Location	Regina, Saskatchewan	Lucky Lake, Saskatchewan	Athabasca, Alberta	The Pas, Manitoba	Pinawa, Manitoba
Site latitude (°N)	50.688	51.154	54.603	53.994	50.163
Site longitude (°W)	104.501	107.264	113.644	100.941	96.066
Site altitude (m)	659	709	693	236	247
Spectral coverage	RGB	630 ± 2 nm	CYGM	Monochrome	Monochrome
Fit type	Gnomonic	Fisheye	Fisheye	Fisheye	Fisheye
Fit epoch (UTC)	5:59:13	05:00:14	06:08:01	5:05:29	4:44:49
Clock offset needed (s)	−165	−2	−1	−2	−1
ISS meridian crossing	8:04:49.9	8:04:22.4	8:03:18.6	8:05:25.5	8:06:14.8
Barrel distortion	Quadratic	Linear	Linear	Linear	None
Gnomonic λ_0 (rad) or Fisheye X_0 (unit circ)	−0.5668	−0.0133	−0.1137	0.0157	−0.0385
Gnomonic φ_0 (rad) or Fisheye Y_0 (unit circ)	0.9905	0.0202	−0.0216	0.0306	0.0145
Scale	0.8311	0.9955	0.9298	0.9337	0.9243
θ_0 (radians)	3.0708	0.0520	−0.0900	0.0113	−0.0314
Bradial or Bx	2.6163	1.206	−0.0558	−0.3935	9.016
By	1.7994	–	0.0434	0.2533	–
Bxx	1.8692	–	7.616	9.1947	–
Byy	1.8747	–	6.5599	4.7683	–
Bxy	0.1375	–	−0.0011	0.6465	–
RMS error (pixels)	1.91	0.55	0.32	0.72	0.72
RMS error (unit circle)	0.00023	0.0026	0.0039	0.0055	0.0057
Pixel resolution	4,912 × 7,360	512 × 512	128 × 256	256 × 256	256 × 256
No. of frames coadded	1	10	10	10	20
Total exposure (s)	4	20	50	10	20
No. of points fit	71	89	38	48	32
No. of parameters	9	5	9	9	5
Red magnitude limit	11.2	–	–	–	–
Green magnitude limit	11.3	–	–	–	–
Blue magnitude limit	10.8	–	–	–	–
Grayscale magnitude limit		3.5 (10 frames)	3.5 (10 frames)	4 (10 frames)	3 (20 frames)
Other REGI epochs	6:07:18	6:07:26	6:07:32	6:07:46	6:07:53
Gnomonic λ_0 (rad)	2.7122	−0.4427	5.5526	−0.6672	−0.3761
Gnomonic φ_0 (rad)	2.6925	0.8511	1.3252	1.9898	2.4390
Scale	0.8311	0.8312	0.8315	0.8292	0.8287
θ_0 (radians)	0.0347	3.1746	2.9196	−0.2262	−0.0450
Bx	1.8953	−1.9047	−1.2762	1.351	1.796
By	−2.8018	2.6374	2.8724	−2.9598	−2.879
Bxx	1.8215	1.8194	1.8613	1.8969	1.9219
Byy	1.7561	1.6856	1.5784	1.6415	1.7590
Bxy	−0.1915	−0.2223	−0.1588	−0.1225	−0.0554
RMS error (pixels)	1.24	1.79	1.39	1.63	1.78

Table 1
Continued

Site designator:	REGI	LUCK	ATHA	TPAS	PINA
RMS error (unit circle)	0.00021	0.00029	0.00021	0.00020	0.00022
No. of points fit	50	66	80	81	63

the ISS is particularly bright, an accurate synchronization of the registered time stamps for each of the ASI cameras can be accurately and precisely determined using the observed meridian crossing times of the ISS in the data from each camera. The clock offset times found in this way that are required to synchronize the four ASIs to the ISS are listed in Table 1. The small ASI clock offset times quantify the accuracy of the current synchronization technique assuming there is no error in the official ASI time stamps.

2.2. Registration Using Bright Stars

Once an accurate synchronization of the image times is in hand, pixels in each image are registered to local angular coordinates of azimuth and elevation using a number of stars in the images. The right ascension (RA), declination (DEC), and magnitude values are taken from the Yale bright star catalog (Hoffleit, 2014). Using the time and geodetic location of the camera for any given photograph, the RA and DEC for all stars in the bright star catalog are converted to local angular coordinates using the starCat2Obs function from Crouse (2017). This function includes corrections for parallax and atmospheric refraction and enables the use of celestial objects observed even near the horizon. A set of clearly identified stars, as well as planets when apparent in the data, are chosen using the Matlab cpselect function. To aid this process, all stars brighter than a specified magnitude limit are plotted as circles with radii proportional to brightness, and the locations seen in the observed data are compared with the predicted locations of the bright stars. Non-linear least squares fitting determines an estimate of the parameters for the observed camera that converts pixel coordinates in the photograph to azimuth and altitude. For the REGI camera a primarily gnomonic projection (Weisstein, 2019) was used. For the ASI cameras with fisheye lenses, a primarily linear equidistant projection (Bettonvil, 2005) was used. For both types of lenses, correction for barrel distortion was required to provide acceptable registration. The Matlab (Mathworks, 2019) functions used for these fits and image registrations, with the explicit definition of the fitting parameters listed in Table 1, are available in the supplemental materials. For each of the four ASI cameras the fit parameters were found to be valid for the full series of images. For the REGI images, a number of different camera orientations were used over the series of photographs, but within any given stable pointing, a single registration was valid. The REGI registration parameters for six different camera orientations are tabulated in Table 1.

Note that the RMS fit error for the REGI data represents approximately 1 arcminute of error in angular position. Without the correction in the present analysis for atmospheric refraction effects (~30 arcminutes near the horizon) the fit error for stars or planets near the horizon would be much greater than 1 arcminute. Since stars at the celestial equator appear to move 1 arcminute in only 4 s, this illustrates the importance of accurate determination of the times of the photographs. At the other extreme of quality, the 20-fold larger fit error for the PINA data is due to the lower sensitivity and much poorer seeing conditions at this site that allowed the use of only a small number of reference stars.

It can be seen from a comparison of the magnitude limit of approximately 11 in all three spectral channels for the digital camera images to the magnitude limit of only three or four for ASI cameras (even with co-adding of 10 or 20 frames) that the digital camera images have far superior sensitivity. It can be seen from the order of magnitude smaller error (in unit circle terms) of the digital camera images that the spatial resolution is also far superior to the ASI images. These sensitivity and resolution advantages make modern digital camera data taken by observers that fortuitously happen to be in the right place at the right time potentially extremely useful, especially with regard to analysis of the sort displayed in Figures 5 and 6 below.

Table 1. The image registration parameters for each of the sites discussed in the text are tabulated here. The site designator four letter acronyms for each site are in row one, followed by information on the locations in the next four rows. The spectral coverage for the camera systems at each site are then listed. The type

of fit involved in the registration process is listed, and the epoch used to generate the expected locations of the stars and planets for use in determining the control points for the registration process. The clock offset needed for bringing the recorded time stamps from each sites' set of data into synchronization with the time of the meridian crossing of the ISS is then listed, together with the meridian crossing time computed from the ISS orbital elements. The nature of the correction for camera lens barrel distortion, either linear or quadratic is listed. The next several rows contain the best fit parameters found to bring the positions of the chosen set of control points into best agreement with their correct values at the fit epoch. The details of the functions of the registration are included in the supplemental materials. At the end of the list of fit parameters, the quality of fit in terms of the RMS error between control points and known values is given both in terms of pixel units and in terms of the "unit circle," in which the local horizon is at unit radius. The format of the images is given in pixels. The number of sequential frames of data coadded in order to improve the signal-to-noise ratio of the data is listed, followed by the number of points used in the fit. The number of parameters for each fit is listed, followed by a quantification of the magnitude of stars that are detectable in the image, either in terms of the separate colors for the REGI case, or in terms of the grayscale level for the other images. The last 13 rows contain the same information for the five different camera orientations used in the panoramic sweep at the times listed.

2.3. Check of Registration Accuracy Using "Maxima Merging" Technique

A check of the end-to-end accuracy of the process of time synchronization and image registration is shown in Figure 1. In this figure, the ASI label and UTC at the time of the ISS meridian crossing over each imager are used as titles for each image. The location of the local horizon is indicated by the large cyan circle. Each photograph is oriented with NORTH at the top and WEST to the right, as explicitly indicated on the ATHA image. Computed ISS locations at 3 s intervals, starting at 8:01:47 (the time that the ISS is first illuminated on this particular orbit by the sun) and ending at 8:09:41 (the time that the ISS reaches the cyan horizon in the LUCK image) are shown by the red dots in Figure 1. Here, for each of the four ASI's, the series of registered images nearest the closest time to the meridian crossing for each camera are combined by "Maxima Merging" (MM) and shown. For every pixel in such an MM image, the maximum intensity value from the series of images being merged is used. As a result, for moving objects, such as the International Space Station, a series of streaks are seen. The length of each individual streak is a function of the exposure time of the camera, the speed of the moving object, the distance to the moving object, and the location of the moving object. It can be seen that the exposure times of each of the four ASI cameras is consistent with the length of the streaks in each merged image. The number of separate images merged is greatest for the LUCK case, as the ISS is observed for the longest time interval (342 s) at this location. The motion of some stars over the 342 s interval in the merged image is also apparent. For the LUCK MM image, near the center of the image, every frame of LUCK data is merged and clearly separated "dashes" are apparent and can be seen to line up well with the location of the ISS red dots. Furthermore, from the center of the LUCK MM image, where the ISS observations become more crowded, either every other, or every fourth LUCK image was merged in order to verify the timing of the ISS observed positions by having clearly separated "dashes." A similar sub-selection of images is used for the ATHA and TPAS contributions to the MM image, in order to clearly associate ISS positions with the observed "dashes," except that because of the inherently poorer resolution of the ATHA, TPAS, and PINA data, even near the center of the image, only every other frame is merged. In the PINA image shown, it was clearly raining at the time of the ISS crossing, the sky was quite cloudy, and the individual ISS images are quite blurry.

The quality of the agreement between the ISS image locations computed purely from the satellite orbital elements and the observed locations in the *registered* ASI images provides an overall validation of the current approach both to the registration of ASI images using stars and planets as well as to the synchronization of images taken from widely spaced cameras that are viewing the same rapidly moving object. This is particularly important for the analysis of dynamic structures, such as the purple bands, and especially the green picket fence posts of STEVE.

Although the ISS was not captured in any of the REGI images, another bright satellite seen in all the ASI cameras (except for PINA because of cloud cover) is NORAD-20436, which is a bit of residual debris from

the SPOT-2 satellite (de-orbited in July 2009). This satellite is also seen in REGI and this allows for the synchronization of its photographs.

In Figure 2, the SPOT-2 debris streaks are indicated, as well as the NORAD-25758 satellite and a meteor. The meteor was captured by both the LUCK and REGI cameras and provides an additional and independent confirmation of the quality of the registration as well as the quality of the synchronization. The REGI image shown has four successive photographs merged, as described above for the ASI images in Figure 1, for the four brightest appearances of the SPOT-2 debris from the REGI perspective. In the case of colored images, the maxima for each color are merged separately. The meteor streak appears in only the 5:54:37 REGI image. The LUCK image shown has three photos (at times indicated in parentheses) merged, corresponding to the brightest appearances in LUCK. The meteor streak appears only in the 5:54:36 LUCK exposure. Similarly, the ATHA image has three bright appearances from the ATHA perspective merged. Only the single TPAS 5:54:38 photo is used, as the cloud cover obscured much of the sky at this time. Superimposed on all four images are a series of red dots, corresponding to the computed position of the SPOT-2 debris at 6 s intervals from 5:54:13 to 5:55:07. Note that the brightness of the SPOT-2 debris exhibits a "flare event" during its passage and varies rapidly as it happens to reflect sunlight toward the different ground stations at differing times. It is found that the error between the computed satellite positions and the observations are in disagreement by approximately 15 km in both the cross track and along-track directions at an altitude of approximately 640 km. It is plausible that the TLEs for this defunct satellite are not as accurate as the TLEs for the ISS, and for this reason, the discrepancy between the predicted and observed track is greater. Considering both the possible TLE errors for the SPOT-2 satellite, as well as timing errors associated with "flaring," the estimated error in the value of the clock offset for REGI using the SPOT satellite debris alone may be more than a few seconds. Ignoring these possible systematic errors, the SPOT debris data leads to an estimated clock offset for REGI of −165 s.

2.4. Parallax Track Analysis of Three-Dimensional Geometry

Based on the SPOT-2 debris-based synchronization of REGI to LUCK, the 5:54:37 REGI exposure, having a duration of 4 s, ended 1 s after the 5:54:36 LUCK exposure of duration 2 s. The exposure of the 5:54:36 LUCK image shown would, therefore, fall entirely within the exposure time of the 5:54:37 REGI image. As a result, the precisely determined locations for the head and tail of the meteor seen in these images can be used to determine the altitude distribution along the track of the meteor using a "parallax track" analysis method. This method is based on triangulation of corresponding objects seen in simultaneous photographs from multiple locations but has the advantage of simplifying the location and identification of objects seen in multiple photographs.

A particular point of interest, such as that marked by the magenta asterisk in the REGI image at the tail of the meteor, corresponds to specific azimuthal and elevation angles from the REGI point of view. This particular point will appear somewhere along a curve in the other imagers, with the location determined by the altitude of the point. Representative locations, spaced at 100 km intervals along the line of sight extending from the camera at the REGI site in the direction corresponding to the magenta asterisk in the REGI image, are indicated by the magenta asterisks shown superimposed on the images from the other imagers. These are labeled "Parallax Tracks." The magenta asterisks in each image are joined by magenta line segments. The altitude of the magenta asterisk point in the REGI image corresponding to the tail of the meteor is determined by the intersection of the magenta parallax track with the observed location of the meteor tail in the LUCK image indicated by the green circle.

Similarly, the cyan asterisks linked by cyan line segments represent the line of sight corresponding to the center of the white circle indicating the location of the meteor head in the REGI image. Just as for the magenta case, the altitude of the cyan asterisk in the REGI image is determined by the intersection of the cyan parallax track with the center of the white circle indicating the head of the meteor as seen in the LUCK imager. Parallax tracks are quite helpful in the process of altitude determination but for clarity are not shown in later figures.

Since the meteor trail extends the full distance between the parallax tracks superimposed on the LUCK image, it is verified that the meteor light occurred entirely within the two s LUCK camera exposure, and

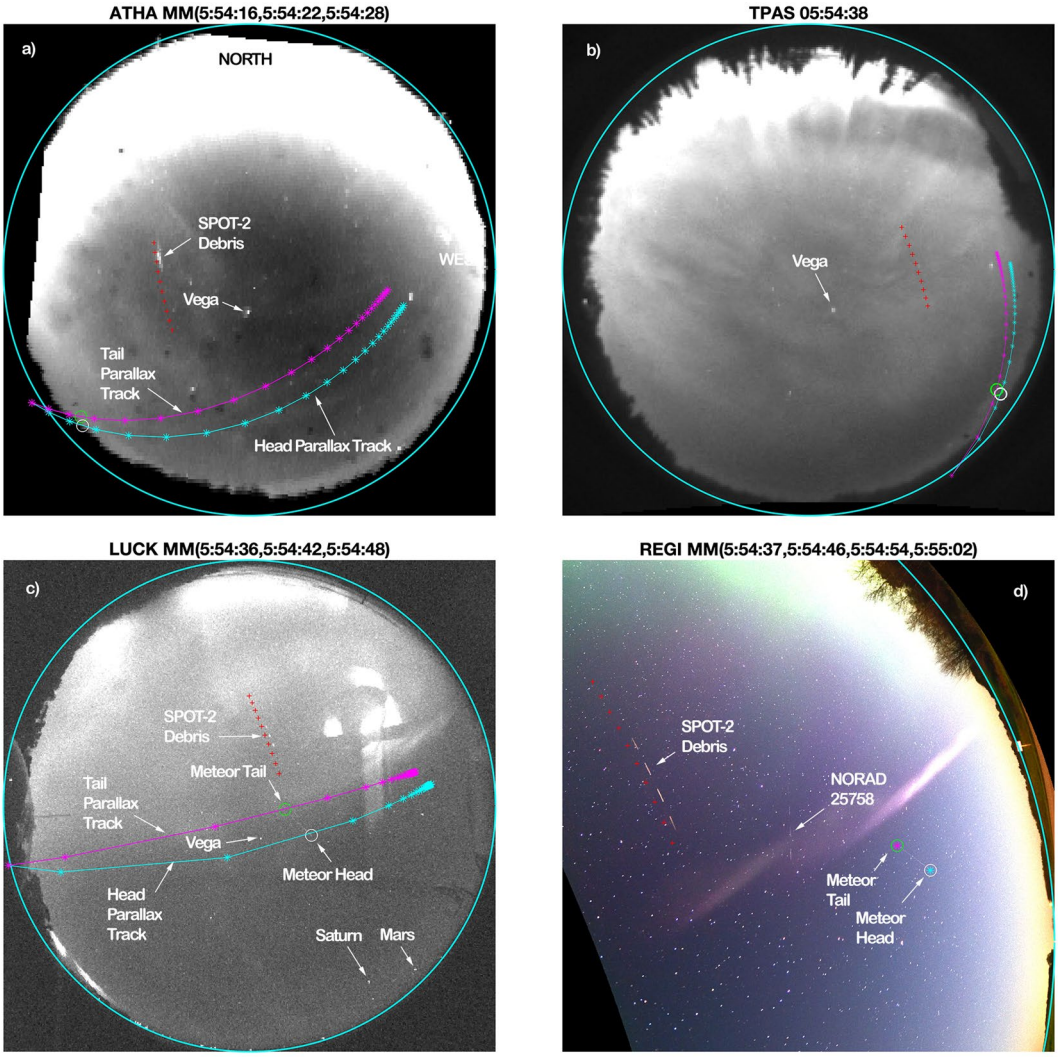

Figure 2. Various images used in the synchronization of the REGI photographs to the ASI photographs are shown here. In (a) a "Maxima merged" MM composite of ATHA images at the three times indicated in the title, in (b) a single TPAS frame, in (c) an MM composite of LUCK images at the three indicated times, and in (d) an MM composite of REGI images at the four indicated times. Moving objects having significant luminosity for a longer duration that the individual camera exposures appear as "dashed lines" in the MM composites. In each image, the computed locations of the SPOT-2 satellite debris at six s intervals are marked with red dots. Moving objects having significant luminosity for a shorter duration than the individual camera exposures appear as single "streaks." The meteor seen in a single LUCK and a single REGI frame provides such an example.

that the LUCK exposure happened entirely within the four s REGI exposure. This allows a lower bound of 18 km/s to be placed on the meteor speed. This speed is well within the normal range of meteoric speeds (Hankey, 2019) of 11 to 72 km/s. The head and tail altitudes, approximately 100 and 130 km, respectively, are also quite reasonable meteoric values. Finally, it can be concluded from the meteor track alone, that the relative clock offsets between REGI and LUCK are accurate to ±1 s.

In the REGI image shown in Figure 2, in addition to STEVE and the green auroral activity, the pair of LEO satellites and the meteor are all simultaneously visible, with an enormously large range of altitudes. The common auroral analysis approach of mapping ASI data to a single altitude is inadequate for the analysis of such images. In contrast, the approach described here involving the use of "parallax tracks" works quite well, provided clear points of interest can be identified in nearly simultaneous images taken from at least two sites at different locations. A parallax track is especially helpful for the location and identification of an object at an unknown altitude in a crowded field. It can be seen, for example, that the meteor was so near

the horizon relative to both ATHA and TPAS, that it would naturally not be expected to be easily detectable in those images.

2.5. Synthetic All-Sky Image Creation From Panoramic Sweep

Figure 3 displays data from a time that a "panoramic" sweep of five photographs was taken across the night sky from the REGI site. These exposures were made sequentially from West to East. The details of these five exposures are listed in the last 13 rows in Table 1. Because the registration errors for these images are so small (the rms error is approximately one arcminute) the MM REGI image effectively produces a synthetic ASI image. In regions of the sky not covered by a given component image, intensity values of zero are used, so such images do not contribute to the MM composite. Intensity and color variation artifacts are noticeable near the edges of some of the sub-images. These edge artifacts are the result of a slight vignette effect from the camera lens. These edge artifacts do not affect the location of features in the composite image. In order to reduce saturation in the MM image, the component images at both horizons were scaled by 50%. In order to cover approximately the same time interval represented in the REGI composite image, as well as to reduce noise, 21 LUCK frames, 21 TPAS frames, and 10 ATHA frames were coadded rather than combined by MM. The time labels indicate the mean time of the coadded images.

Superimposed on the LUCK, ATHA, TPAS, and REGI images is a grid of magnetic field line vertices joined by line segments shown in green. The magnetic field was computed using the enhanced magnetic model (EMM) Matlab code from Crouse (2017). This EMM model uses an order 720 spherical harmonic expansion (Maus, 2010) to represent the earth's magnetic field. The values of the magnetic field computed with this model were compared with the entire day's series of 86,400 SWARM satellite measurements. The maximum difference in direction between the EMM calculated field and the SWARM measured field over the entire day was 0.93° and the largest differences were seen as the satellite passed through regions of auroral activity. In the subauroral vicinity of the STEVE overpass shown in MacDonald et al. (2018) the maximum difference between the EMM model and the SWARM measured field in direction was only 0.06° and this angular difference *changed* by only 0.02° as STEVE was crossed. The magnetic field line passing through any particular point in space can be traced up or down in space by following the local direction of the EMM magnetic field and can be uniquely identified by the centered dipole (CD) coordinates of magnetic latitude and longitude of the "foot of the field line" where such a tracing reaches the nearest zero altitude location with respect to geodetic coordinates.

The series of magnetic field line vertices shown lie at altitudes of 190 and 250 km. They are shown at intervals of 2° in magnetic longitude from 24° to 62° west, as indicated by the white labels next to some of the magnetic longitude lines. Note that the higher altitude 250 km grid lines lie to the north of the 190 km grid lines from the ATHA and TPAS perspectives, but to the south from the REGI and LUCK perspectives.

The parameters for a linear fit of the magnetic latitude versus longitude for the prominent STEVE emission in this figure are shown in Figure 3a with the assumption that the altitude range is 190–250 km throughout the scene. Although slight "wiggles" about the purely linear fit are apparent in the data, as most clearly seen in the LUCK 06:07:48 image in Figure 3c or the REGI image in Figure 3d, the departures are no more than 0.1° in terms of a latitude variation. Alternatively, if not departures in latitude, the "wiggles" interpreted in terms of an altitudinal variation would be no more than 50 km at the most extreme. Although the variation of magnetic latitude versus longitude at a typical auroral oval boundary could be curved rather than linear over a 40° span of longitude, a purely linear fit was all that was warranted here.

In addition to the synthetic ASI image comprised of a Maxima Merging of successive registered REGI photographs near 6:07:48 shown in Figure 3d, several other MM composite images could be formed. Every time successive photos were taken with significantly different aim points of the camera useful MM composites can be formed.

2.6. Intermittency of Green Picket Fence Posts

Before the time of the images shown in Figure 3, a number of green "picket fence post" features began to appear in the REGI data as can be clearly seen in Figure 4d. The original, unregistered 6:01:06 REGI image

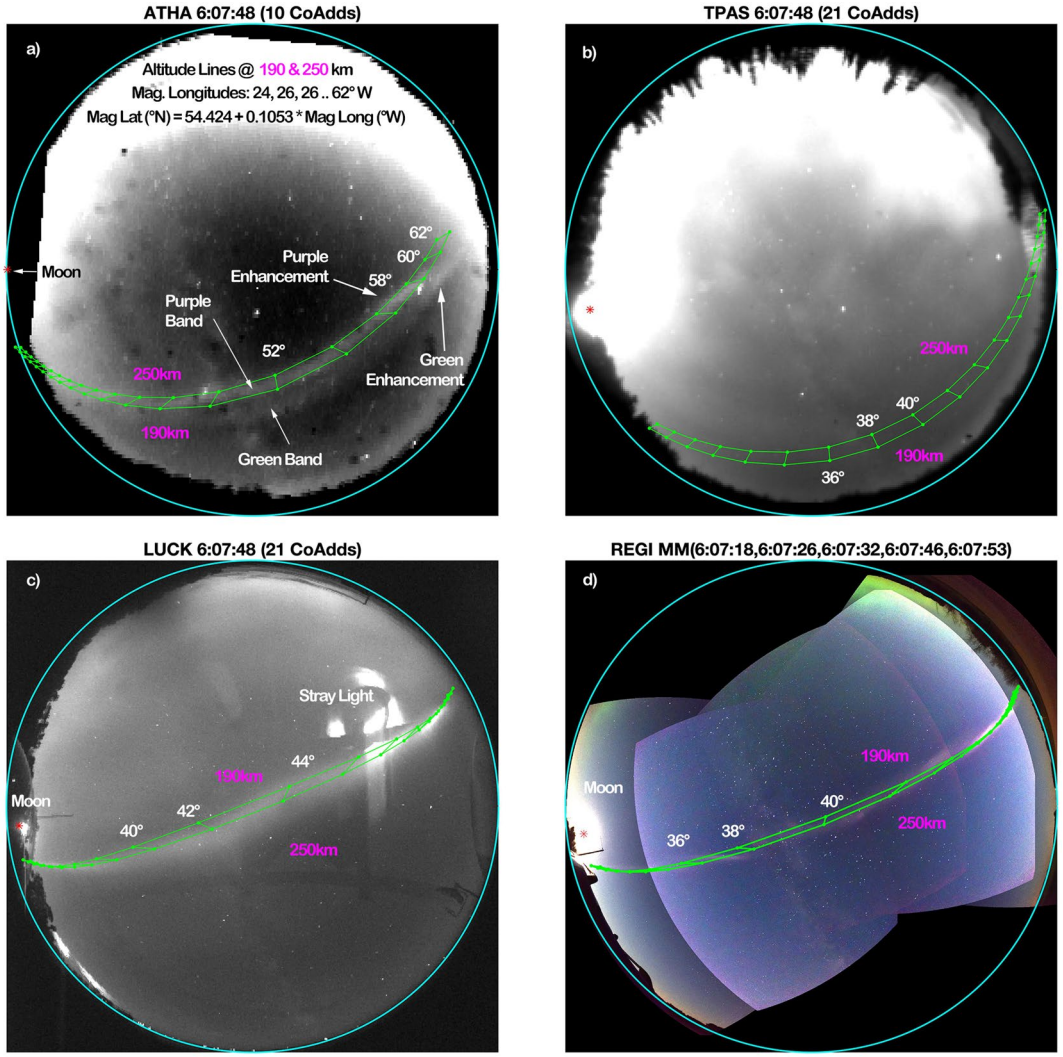

Figure 3. Co-added ASI images from ATHA, TPAS, and LUCK at 6:07:48 are shown in (a), (b), and (c) respectively. In (d) is shown a synthetic All-Sky image created from the "Maxima Merged" composite of five REGI photographs from the times indicated in the heading. A grid of vertices linked by line segments at altitudes of 190 and 250 km for coordinates at 2° steps in magnetic longitude, with latitudes following the linear relation shown in (a) is shown in green superimposed on all images. Selected longitudes are indicated in white numerals on each image. The band of STEVE luminosity clearly visible in LUCK and REGI closely follows the green grid. In ATHA, two separate streaks of luminosity are seen, labeled as the purple and green bands, but only the purple band follows the green grid.

used here is exactly the same as the central frame published in Figure 1 of MacDonald et al. (2018) but labeled there with the *incorrect* time 06:03:51 UTC. These green features are also seen in the ATHA data, but the colored images are quite noisy, and it is preferable to use grayscale ATHA images (produced by summation over the four color channels of the original ATHA data) to observe their spatial structure. The full color (University of Calgary, 2020) ATHA keogram spanning the 6:00 to 6:59 time interval displayed in Figure 4b confirms the difference in color seen far more clearly in the REGI image between the upper and lower structures. The vertical scale of the keogram is displayed so that it conforms to the vertical extent of the grayscale ATHA image to the left. As Vega passes across the center of the ATHA imager it produces the rainbow-colored streak artifact seen near 6:45 in the keogram. In the keogram spanning the 6:00 to 6:59 time interval, it is seen that one band has a greenish tinge, while the other band has a purple hue. In the REGI image at 6:01:06 shown, several distinct "green picket fence posts" are seen near the center of the image. Occasionally, some of these posts are bright enough to be individually discernable in the ATHA data, but with far less resolution. From successive REGI images, it is found that the individual green picket fence

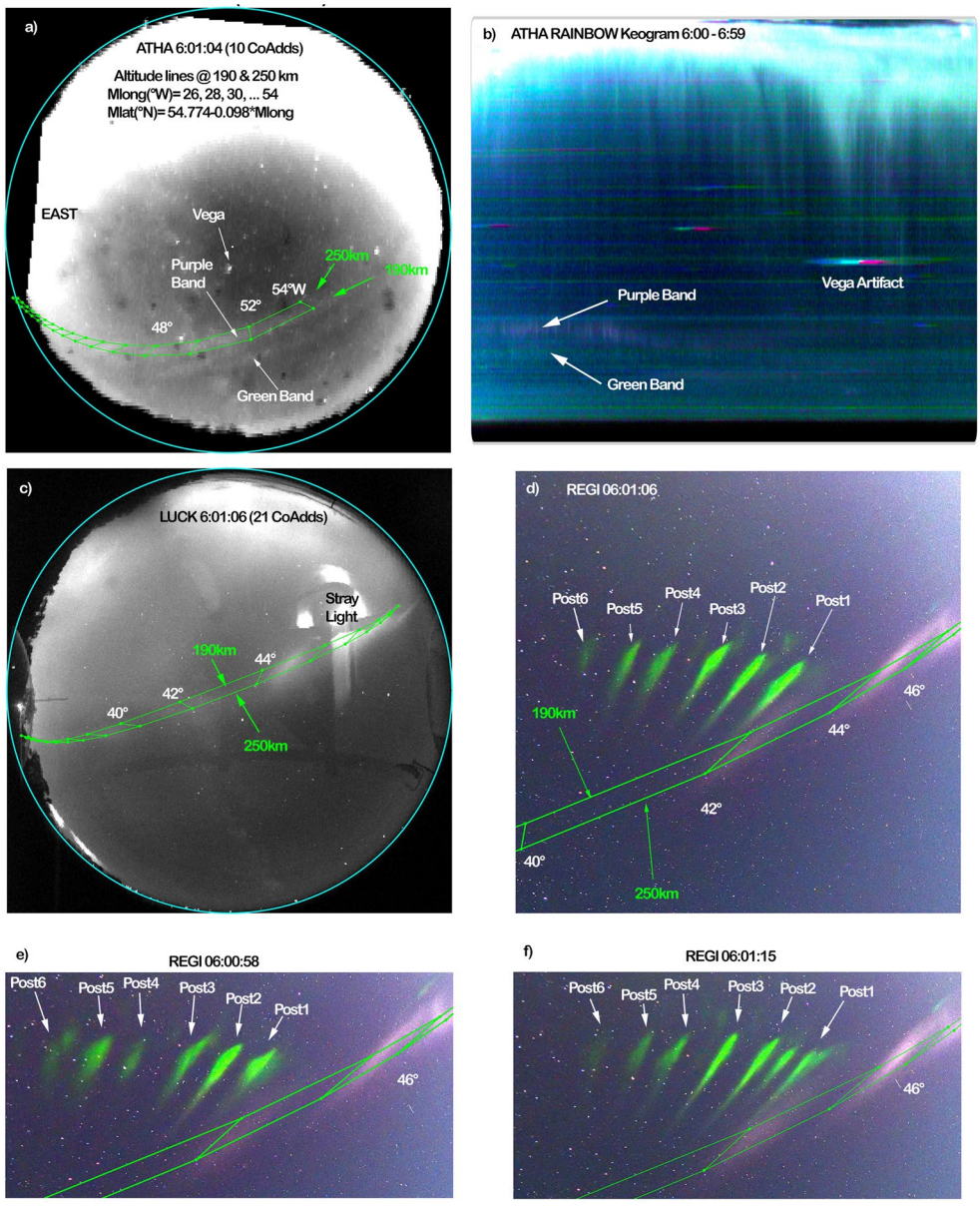

Figure 4. STEVE features are seen simultaneously in (a) ATHA, (c) LUCK and REGI. An ATHA keogram is shown in (b). Six green picket fence posts are indicated in (d–f). A grid of magnetic field line segments is shown in green. The specific green grid shown is chosen to pass through the purple band of luminosity seen in all three imagers and is the same fixed grid in all six panels of this figure.

posts vary significantly from frame to frame. The intermittency of the picket fence posts is also apparent in the ATHA keogram.

The intermittency of the picket fence posts seen also accounts for the observation that while there appears to be a nearly continuous band of green luminosity extending from horizon to horizon seen in the coadded ATHA image shown in Figure 3a there is no discernable evidence of green posts in the MM composite REGI synthetic ASI shown in Figure 3d despite the far greater sensitivity to the green posts in the REGI data. The reason for this difference is attributed to the fact that the 10 coadded ATHA frames represent an average over a 60 s period, while the individual REGI frames each had an exposure of only 4 s. Just by happenstance, none of the five individual REGI frames involved in the composite MM image captured green picket fence posts, even though they are clearly visible in a REGI photo taken just 22 s before the first frame of the panoramic sweep shown in Figure 3d).

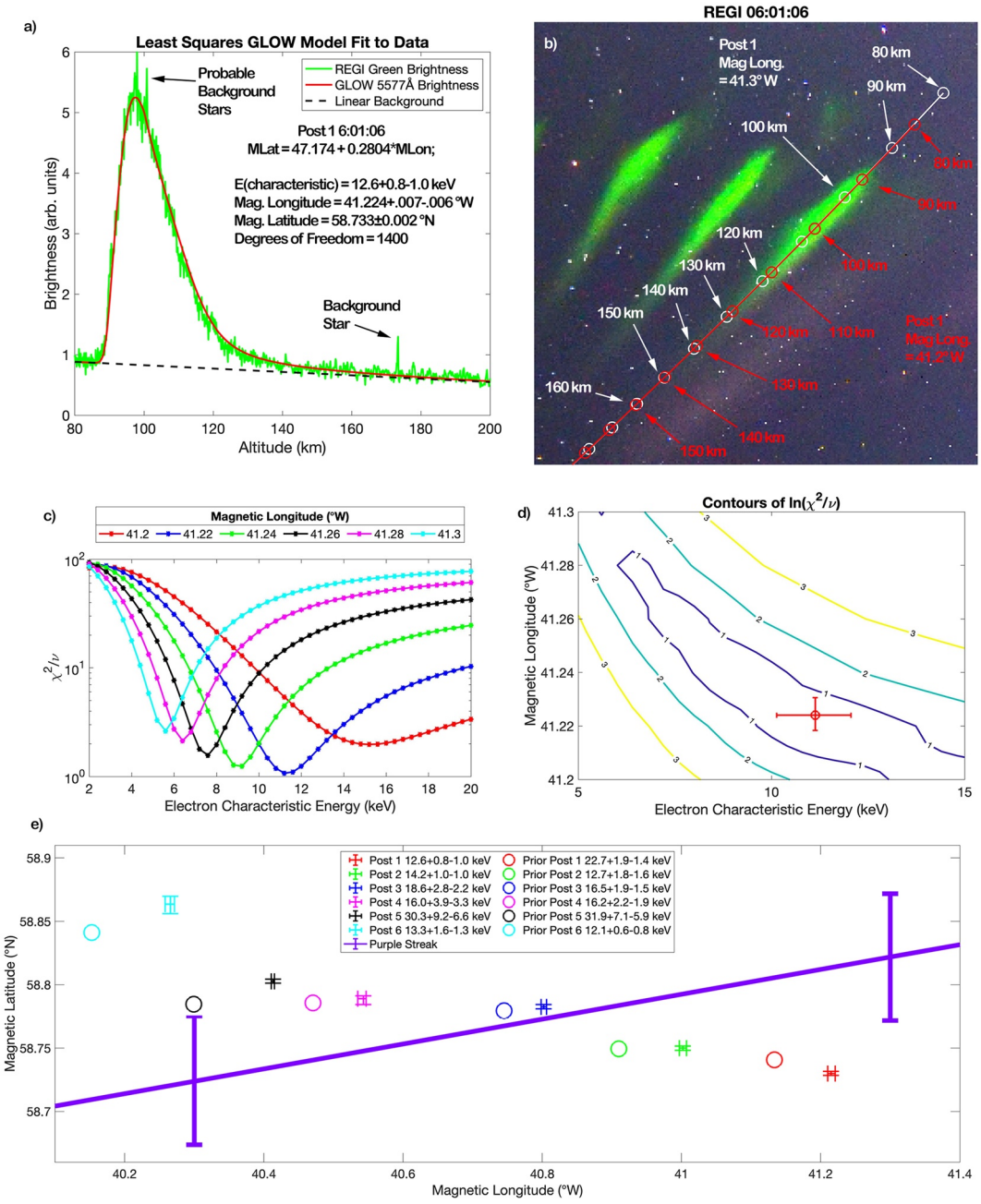

Figure 5. The least squares fitting of Post one to a linear background plus GLOW model is illustrated here. In (b), the location of two exemplary magnetic field lines passing through the middle of Post one are shown in red and white. The locations in the image of points at altitudes from 80 to 200 km at 10 km intervals along the two field lines are indicated to illustrate the sensitivity of the derived intensity versus altitude function to the choice of magnetic field line. In (c), for each of six specific choices of magnetic longitude, the χ^2 / υ is plotted as a function of the GLOW model characteristic energy. In (d), a contour plot of $\ln(\chi^2 / \upsilon)$ is plotted as a function of energy and longitude. The red circled point represents the best fit value, with horizontal and vertical error bars representing the one-sigma uncertainty in energy and longitude respectively. The degree of covariance between these two variables can be seen by the slope in the "valley." In (a), the GLOW model calculation for the best fit case is shown, together with the fit parameters and uncertainties. In (e), the best fit results for each of the six posts shown in Figure 4d are plotted with horizontal and vertical error bars shown. Also plotted as circles are the best fit results for each of the six "prior" posts shown in Figure 4e corresponding to the photograph taken 8.34 s earlier. Finally, the location of the magnetic grid that best aligns with the swath of the purple streak of luminosity across ATHA, LUCK and REGI seen in Figure 4 is shown in 5e by the purple line and error bars in the region of the six posts.

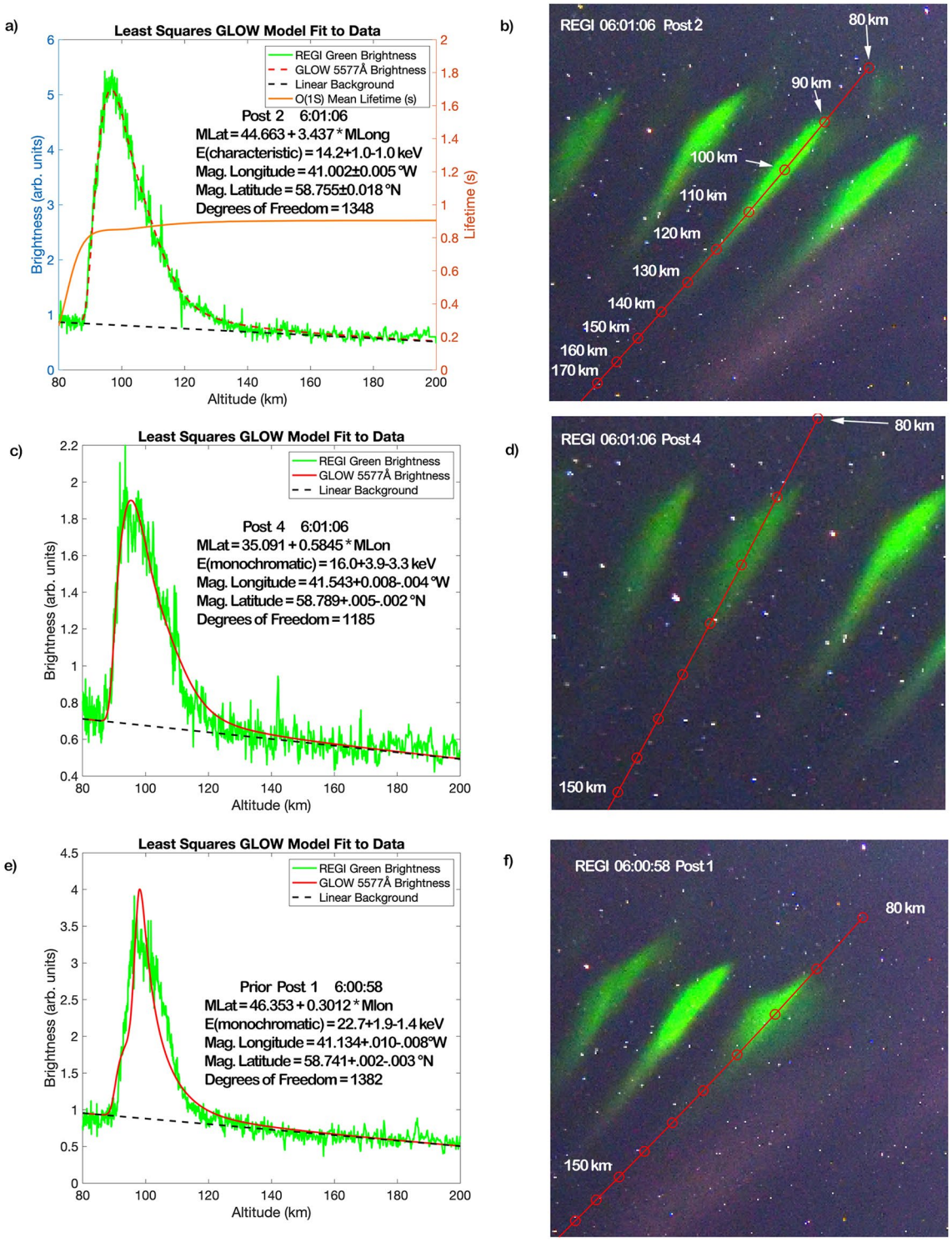

Figure 6. Details for three posts are shown. In (a), for post 2 at 6:01:06, the best fit case is displayed for a Maxwellian distribution. The locations of the best fit magnetic field line coordinates at altitudes from 80 to 200 km are displayed by the red line and circles superimposed on the observed data in (b). Similar fits using Monochromatic electron energy distributions are shown for Post 4 at 6:01:06 in (c) and (d) and for Post 1 at 6:00:58 in (e) and (f).

2.7. Exploitation of Magnetic Field Aligned Structures

The green picket fence post features appear very well aligned with the local magnetic field lines. The quality of this alignment is best seen by the closeup regions of REGI data in Figures 5b, 6b, 6d, and 6f. Although it is conceivable that the green picket fence post features are not actually field aligned structures but are instead all at a common altitude (say) but just by happenstance spatially distributed so that they only "appear" to be aligned with the local magnetic field, in view of the fact that numerous independent "posts" appear fleetingly from frame to frame, and that so many of these posts are just as well aligned with local field lines as the cases explicitly shown in Figure 4d, it seems highly unlikely that these posts are NOT field aligned. In a later section, a few cases in which the green posts are not so well aligned with local magnetic field lines will be shown and discussed.

The presence of magnetic field aligned features allows another independent approach to the determination of three-dimensional structure that is illustrated in Figure 5. In this approach, it is assumed that the green intensity seen in the REGI data can be attributed to the excitation of the 5577 Å spectral line by a population of precipitating electrons. High spectral resolution measurements of green picket fence features by (Gillies et al., 2019) show that the assumption of dominance for the 5577 Å emission is reasonable. That this emission is produced by precipitation rather than ionospheric skyglow is a topic of debate in the current literature, as summarized in the introduction. Here, we explore the ramifications of the assumption that this emission is in fact produced by electron precipitation.

The "global airglow" (GLOW) model (Solomon, 2001; Solomon et al., 1988) is used to compute the volume emission rate as a function of altitude emerging from a population of precipitating electrons initially descending along a particular magnetic field line. We will consider both a Maxwellian energy distribution and a Monochromatic energy distribution for the incoming electrons at the top of the atmosphere. In order to relate the observed brightness along the length of a given green fence post to the brightness as a function of altitude, it is necessary to determine the relation between the position in the image of a given region of luminosity and the altitude of said luminosity.

Requiring that a magnetic field line passes through a fixed point in a given photograph, such as a point near the center of a particular green fence post, constrains the relation between magnetic latitude and longitude. Over the range of coordinates considered here, this constraint produces a linear relation between the latitude and longitude. For the case shown in Figure 5b this relation is

$$\text{Magnetic Latitude}\left(^{\circ}\text{N}\right) = 47.174^{\circ} + 0.2804 \times \text{Magnetic Longitude}\left(^{\circ}\text{W}\right). \quad (1)$$

The linear coefficients vary strongly with the specific fixed-point choice. The values used for the other representative posts shown in Figures 6b, 6d, and 6f are listed along with the resulting best fit parameters shown in Figures 6a, 6c, and 6e.

A specific choice of magnetic longitude then leads to a specific relation between the position along the field line and the altitude of that point. An illustrative example of these relations for the picket fence post radiolabeled "post one" in Figure 4d is shown in Figure 5b. The field line having magnetic longitude 41.3 W passing through the center of post 1 is shown in white, with white circles for altitudes at intervals of 10 km from 80 to 180 km indicated. The alternative field line having magnetic longitude 41.2°W also required to pass through the center of post 1 is shown in red, with red circles at altitudes 80 through 170 km shown.

The trajectories of these two field lines are virtually indistinguishable over the region shown in the figure. For the case shown, only at the top of the figure can the red and white magnetic field lines be seen to very slightly differ. Note that the altitude corresponding to a particular location is a very sensitive function of the choice of field line. For any given magnetic field line, the coordinates in the registered camera space are transformed by inverse gnomonic projection back to coordinates in the original photographic image using a piecewise linear interpolation between the locations of the vertices of the magnetic grid coordinates spaced by 10 km in altitude, such as those shown in Figure 5b). The numerical value of the observed intensity at any given altitude is determined by "nearest neighbor" interpolation along the piecewise linear inverse gnomic projection path through the original photographic data.

For six magnetic longitude choices evenly spaced between the extremes shown in Figure 5b, a series of least squares fits of GLOW model calculations to the observed luminosity were made with characteristic electron energies ranging from 0.4 to 20 keV in steps of 0.4 keV. The intensity along a given field line was extracted and converted to the intensity as a function of altitude. Inconveniently located bright stars can sometimes not be avoided, and the observed intensity near such stars (typically only a few pixels out of approximately 1,400 pixels, depending on the choice of field line) is replaced with a value linearly interpolated from the surrounding neighborhood. The number of degrees of freedom for the fit is reduced by the number of such "patched" pixels. For a given magnetic field line and characteristic electron energy, the three fitting parameters were: a slope and offset for the assumed linear background and an electron flux level for the strength of the GLOW model calculation.

The sum of squared residuals normalized per degree of freedom χ^2 / υ is plotted for each of these fits in Figure 5c. A contour plot of χ^2 / υ is plotted in Figure 5d as a function of the electron characteristic energy and magnetic longitude. A noise level common to all fits displayed in 5c and 5d was chosen to make the overall minimum χ^2 / υ be unity. This noise level includes not only the camera readout noise and photon shot noise, but also the "clutter" noise from the host of underlying stars and other celestial objects that might underlie the region of green post luminosity. The minimum χ^2 / υ determines the best fit values for the electron energy and the magnetic longitude. The best fit GLOW model, assuming a Maxwellian energy flux distribution, is compared with the observed brightness as a function of altitude corresponding to the best fit magnetic field line coordinates in 5a. In this plot, no correction for the "background" star appearing just above the 170 km altitude level, nor for the pair of likely stars located near the peak intensity. Although bright star contamination can easily be detected and "patched" over, dimmer background stars are not so easily removed. For this reason, the "clutter noise" of unresolved background stars is usually larger than the noise from background dark current fluctuations. All this said, the residuals between the GLOW model fit plus linear background and the observed REGI green brightness are approximately normally distributed, with the occasional isolated bright star outliers, so that the "one sigma" uncertainties in both characteristic energy and magnetic longitude may be estimated from the point at which χ^2 increases by $\sqrt{2\upsilon}$ above its minimum value. These uncertainties are not necessarily symmetric about the best fit value. These best fit values and uncertainties are numerically shown in 5a and indicated with the red circle with horizontal and vertical error bars in 5d.

Note that this method for determination of the altitude distribution of STEVE intensity using magnetic field aligned structures in the REGI data is completely independent of the triangulation approach described above. In contrast to the triangulation approach it can be performed using data from a single high-quality digital photograph without the requirement of data from another site. It is only required that the model used, for example, GLOW, produces a reasonable estimate for the variation of brightness as a function of altitude. The altitude distribution found in this way is in good agreement with the altitude range found using triangulation between simultaneous images taken from separate locations, such as the example shown in Figure 4.

A similar analysis for posts 2 through 6 of Figure 4d seen at 6:01:06 leads to the points plotted with horizontal and vertical error bars in Figure 5e. Also shown in this figure are prior versions of posts 1 through 6 in Figure 4e seen at 6:00:58 but plotted as circles having the same color as the error bar plots for the presumably later versions of the same posts. For some posts, the Maxwellian energy distribution assumption produces a brightness distribution that is too broad in altitude to provide an acceptable fit to the observed brightness distribution. Such a case is post 4 at 6:01:06 shown in Figure 6c. Instead, a GLOW model assuming a Monochromatic energy distribution incident at the top of the atmosphere produces a narrower peak, and the fit to the observed brightness is much better. In other cases, neither the Maxwellian nor Monochromatic distributions provide acceptable fits, as can be seen for the prior version of post 1 seen at 6:00:58 shown in Figure 6e. In this case, the observed REGI brightness appears to be broader than a purely Monochromatic distribution, but narrower than a purely Maxwellian distribution.

Qualitatively, the posts seen in Figures 4d, 4e, or 4f that are best fit with Maxwellian distributions appear as more extended streaks with long tails, while those that are best fit with Monochromatic distributions appear as less extended streaks, such as "prior" posts 1, 4, and 6 seen at 6:00:58. Whether a Maxwellian or Monochromatic energy flux distribution is used in fitting, the deduced magnetic field line coordinates

are not significantly affected. In any case, the quite well-defined magnetic coordinates of the green posts strongly overlap with the less precisely determined magnetic coordinates of the swath of purple STEVE luminosity. The green posts appear to share magnetic field lines with the purple streaks, even though not at the same time.

Although there are certain regions where the purple band of luminosity appears to be approximately aligned with local magnetic field lines, there are other regions where the purple band is clearly not so well aligned. In Figure 4d, for example, just west of the 44° line of longitude, a patch of purple seems to extend approximately parallel to the local magnetic field lines. However, just to the west of the 46° line of longitude there is a streak of purple brightness that seems to be nearly at right angles to the local magnetic field lines. This pattern of alignments is also apparent in Figures 4e and 4f. Without confidence that the purple streaks of STEVE are field aligned, an attempt to perform an analysis using the GLOW model similar to that done for the green fence posts is problematic.

2.8. Temporal Analysis of Photographs

Assuming the validity of the GLOW model approach, some of the variations in the shape of specific green picket fence posts observed in the individual images can be interpreted in terms of underlying temporal variations. The GLOW model prediction for the mean lifetime of the O(1S) state responsible for the 5577 Å emission is plotted as a function of altitude as the orange curve in Figure 6a). For all altitudes of interest, the O(1S) state lifetime is less than the 4 s exposure time and 8.34 s cadence of the REGI images shown in these figures. For this reason, the 5577 Å oxygen atomic emission seen in successive images are coming from O(1S) excitations occurring during (or slightly earlier than) the exposure durations of each separate image. In effect, each frame containing 5577 Å emission serves as a "streak camera" image that can provide detailed temporal information at a much finer time scale than the exposure time of the individual images. As an example, the "blurring" seen to the right of the brighter end of Post one in Figure 4f can be interpreted as "motion blurring" as the precipitating electrons responsible for the green emission follow a series of magnetic field lines at successively further westward longitudes. Similarly, the blurring seen to the left of the bright end of Post four in Figure 4f can be interpreted as emission happening somewhat earlier than the stronger emission along the brightest portions of Post 4.

The speed of the apparent longitudinal motion of the precipitating electrons responsible for posts one through six can be quantified by the separation in Figure 5e between the prior versions and later versions of each post. The average longitudinal motion for the six posts corresponds to a longitudinal speed of 0.0115°/s, or a translational speed of 0.67 km/s at the altitude of the posts. This electron drift speed is an order of magnitude less than the ion drift speed measured by the SWARM-A satellite as it crossed over a region of STEVE emission at 6:43:22 as reported in (MacDonald et al., 2018).

A movie of the registered ATHA imagery from 6:00:00 to the time of the SWARM overpass at 6:43:30 is included in the supplemental materials. The motion of various "blobs" in the ATHA movie, such as the localized enhancement of the "green" and "purple" bands shown in Figure 3a), is roughly consistent with the longitudinal speed of the green posts near 6:01 shown in Figure 4. However, the drift speed of the blobs varies and is sometimes greater and sometimes less than 0.67 km/s. The blob drift speeds also sometimes vary from place to place in the ATHA field of view. In order to more readily notice these variations in speed, a moving magnetic grid is displayed superimposed over the ATHA movie. The vertices in this grid move westward in longitude at a constant speed of 0.0115°/s. The vertices also move southward in latitude at a constant speed of 2.5×10^{-4} /s. Over the entire period there are four altitude levels shown: 120 and 160 km in green, 190 and 250 km in red.

3. Summary

We have found that a wealth of data can be extracted from digital images recorded by photographers who have fortuitously been able to photograph night sky events of a rare and transient nature, as typified by the skyglow phenomenon known as STEVE. Stars and planets seen in the images may be used to register pixels

to angular coordinates of altitude and azimuth to within an arcminute. Satellites that appear in the images may be used to synchronize, or check the synchronization of, photographs to within one second.

Application of these methods to the analysis of the July 25, 2016 STEVE event leads to a confirmation of the "double layer" altitude structure of the purple and green streaks previously reported in the literature. From the high spatial resolution photographs, we are able to quantify the energy of the electrons responsible for the green streaks to high precision. We are also able to quantify the apparent speed of the green streaks. Finally, we have found that the green streaks appear and disappear in a correlated fashion over a very broad horizon to horizon swath of longitudes.

As advice to citizen science auroral photographers on how to provide the most useful series of images for scientific analysis, it is quite helpful to have the following:

1. A time lapse sequence using a tripod, with fixed camera settings
2. A panorama across the sky with fixed exposure settings
3. At least one photograph containing the International Space Station for accurate time synchronization, or alternatively a well-defined time stamp
4. Accurate knowledge of the geodetic coordinates from which the images are taken, or if the camera has built-in GPS, a well-defined location stamp
5. Finally, if an unusual event of any sort is captured, please find a relevant scientific organization that can archive your data for distribution and for posterity

With this information, there is no doubt that high resolution, high sensitivity ground-based photographs of STEVE will continue to provide valuable scientific contributions to our understanding of these fascinating events.

Data Availability Statement

The 16-bit registered REGI photographs used in this work are available from https://doi.org/10.6084/m9.figshare.11674206 (Bennett, 2020, Registered Photographs from "Improved Analysis of STEVE Photographs" JGR Article, 2020).

Acknowledgments
The authors declare no competing interests. The image processing functions used to register the photographs discussed in this work are included in the supplemental information.

References

Aida, S. (2013). *Accuracy assessment of SGP4 orbit information conversion into osculating elements*. Paper presented at 6th European Conference on Space Debris, Darmstadt, Germany, ESA.

Archer, W. E., St-Maurice, J. P., Gallardo-Lacourt, B., Perry, G. W., Cully, C. M., Donovan, E., et al. (2019). The vertical distribution of the optical emissions of a Steve and Picket fence event. *Geophysical Research Letters*, *46*, 10719–10725. https://doi.org/10.1029/2019GL084473

Bennett, C. (2020). *Registered photographs from "improved analysis of STEVE photographs" JGR article*. Retrieved from https://figshare.com/articles/Registered_Photographs_from_Improved_Analysis_of_STEVE_Photographs_JGR_Article/11674206

Bettonvil, F. (2005). Imaging fisheye lenses. *WGN, Journal of the International Meterior Organization*, *33*(1), 9–14.

Chu, X., Malaspina, D., Gallardo-Lacourt, B., Liang, J., Andersson, L., Ma, Q., et al. (2019). Identifying STEVE's magnetospheric driver using conjugate observations in the magnetosphere and on the Ground. *Geophysical Research Letters*, *46*, 12665. https://doi.org/10.1029/2019GL082789

Crouse, D. F. (2017). The tracker component library: Free routines for rapid prototyping. *IEEE Aerospace Electronic Systems Magazine*, *32*(5), 18–27. https://doi.org/10.1109/maes.2017.160215

Gallardo-Lacourt, B. L., Liang, J., Nishimura, Y., & Donovan, E. (2018). On the origin of STEVE: Particle precipitation or ionospheric skyglow? *Geophysical Research Letters*, *45*(16), 7968–7973. https://doi.org/10.1029/2018GL078509

Gillies, D. M., Donovan, E., Hampton, D., Liang, J., Connors, M., Nishimura, Y., et al. (2019). First observations from the TREx spectrograph: The optical spectrum of STEVE and the Picket fence phenomena. *Geophysical Research Letters*, *46*, 7207–7213. https://doi.org/10.1029/2019GL083272

Hankey, M. (2019). *Meteor FAQS*. Retrieved from https://www.amsmeteors.org/meteor-showers/meteor-faq/#3

Hoffleit, D. (2014). *Yale bright star catalog*. Retrieved from http://tdc-www.harvard.edu/catalogs/bsc5.html

Kelso, T. (2019). *CelesTrak home page*. Retrieved from https://celestrak.com

Lodriguss, J. (2020). *Nikon D810a review*. Retrieved from http://www.astropix.com/html/i_astrop/eq_tests/Nikon_D810a_Review.html

MacDonald, E. A., Case, N. A., Clayton, J. H., Hall, M. K., Heavner, M., Lalone, N., et al. (2015). Aurorasaurus: A citizen science platform for viewing and reporting the aurora. *Space Weather*, *13*, 548–559. https://doi.org/10.1002/2015SW001214

MacDonald, E. A., Donovan, E., Nishimura, Y., Case, N. A., Gillies, D. M., Gallardo-Lacourt, B., et al. (2018). New science in plain sight: Citizen scientists lead to the discovery of optical structure in the upper atmosphere. *Science Advances*, *4*, eaaq0030. https://doi.org/10.1126/sciadv.aaq0030

Mathworks. (2019). *Mathworks*. Retrieved from mathworks.com

Maus, S. (2010). An ellipsoidal harmonic representation of Earth's lithospheric magnetic field to degree and order 720. *Geochemistry Geophysics Geosystems*, *11*(6). https://doi.org/10.1029/2010GC003026

Mende, S. H. (2019). Subauroral green STEVE arcs: Evidence for low-energy excitation. *Geophysical Research Letters*, *46*, 14256–14262. https://doi.org/10.1029/2019GLO86145

Nikon. (2019). *Download center*. Retrieved from https://downloadcenter.nikonimglib.com/en/products/162/Capture_NX-D.html

Nishimura, Y., Gallardo-Lacourt, B., Zou, Y., Mishin, E., Knudsen, D. J., Donovan, E. F., et al. (2019). Magnetospheric signatures of STEVE: Implications for the magnetospheric energy source and interhemispheric conjugacy. *Geophysical Research Letters*, *46*, 5637–5644. https://doi.org/10.1029/2019GL082460

Solomon, S. C. (2001). Auroral particle transport using Monte Carlo and hybrid methods. *Journal of Geophysical Research*, *106*, 107–116. https://doi.org/10.1029/2000JA002011

Solomon, S. C., Hays, P. B., & Abreu, V. J. (1988). The auroral 6300 Å emission: Observations and modeling. *Journal of Geophysical Research*, *93*, 9867–9882. https://doi.org/10.1029/JA093iA09p09867

University of Calgary. (2018). *UofC space physics data portal*. Retrieved from https://data-portal.phys.ucalgary.ca

University of Calgary. (2020). *UofC space physics group data landing page ground-based observations*. Retrieved from http://data.phys.ucalgary.ca/sort_by_instrument/all_sky_camera/GO-Canada_AGO/stream2.colour_corrected/2016/07/25/atha_rainbow-01/ut06/20160725_06_atha_rainbow-01_full-keogram.pnm.jpg

Weisstein, E. (2019). *Gnomonic projection*. Retrieved from http://mathworld.wolfram.com/GnomonicProjection.html